Advances in Science and Technology Research Journal

*Advances in Science and Technology Research Journal*, 2027, 21(1), 441–460
https://doi.org/10.12913/22998624/236043
ISSN 2299-8624, License CC-BY 4.0

Received: 2026.08.19
Accepted: 2026.11.15
Published: 2026.12.01

# Applicability range of the bending–bimoment analogy in restrained torsion of open thin-walled steel members

Hong Son Nguyen[1], Le Thuy Nguyen[1*], Thanh Huu Le[1], Ngoc Anh Vu[1], Thuy Van Tran Thi[1]

[1] Hanoi Architectural University, 129 Tran Phu, Hanoi, Vietnam
* Corresponding author's e-mail: thuynl@hau.edu.vn

## ABSTRACT

Several steel design codes require the bimoment B in the strength interaction check for open thin-walled members, yet none specify how B is obtained from the applied loading. One long-standing remedy approximates the bimoment diagram directly from the bending-moment diagram; a recent tabulated form of this bending–bimoment analogy, validated against nine classical schemes, reports a maximum error of 4.6%, but only for cold-formed sections with flexural-torsional parameter k ~ $10^{-4}$–$10^{-3}$ $cm^{-1}$. The novelty of this study is to re-examine the analogy's applicability range with an independently verified toolchain closed-form Vlasov solutions for four schemes, cross-checked against a purpose-built two-node torsion finite element and to show that the analogy's relative error is a universal function of the single dimensionless parameter k·L, independent of section geometry, material or load, so that one applicability chart serves any open thin-walled section and scheme. Applied to a hot-rolled channel (k ≈ 0.02 $cm^{-1}$), the analogy exceeds a 5% tolerance beyond k·L = 1.8–3.2 (≈ 0.74 for cantilevers), reaching 22–55% at k·L ≈ 8, typical of hot-rolled spans. For a comparable cold-formed channel, three of the four schemes remain accurate at ordinary purlin spans, but the cantilever scheme already exceeds tolerance there, a scheme-dependent sensitivity not previously reported. A representative strength check shows that neglecting the bimoment altogether overestimates the allowable load by up to 24.2% at the reference section, and by as much as 114% for other schemes, showing that the practical risk of omitting B outweighs the accuracy question addressed by the analogy itself.

**Keywords:** bimoment, restrained torsion, open thin-walled section, warping torsion, finite element method, channel section, cold-formed steel, hot-rolled steel, bending–bimoment analogy.

## INTRODUCTION

Open thin-walled cross-sections channels, I-sections with unequal flanges, Z-sections, and cold-formed lipped profiles are widely used in steel construction because of their favourable strength-to-weight ratio, and their structural behaviour under bending, torsion and combined loading is treated at length in standard steel design references [1]. When such members are subjected to torsion, the assumption of free (Saint-Venant) torsion is, in general, not valid: any restraint against warping of the cross-section, whether provided by a support, a rigid connection, or simply the continuity of the member itself, gives rise to an additional self-equilibrated system of normal stresses known as the bimoment, B. Unlike the bending moment or the axial force, the bimoment has no direct physical analogue in elementary beam theory; it is defined through the sectorial coordinate ω of the cross-section and enters the normal stress as an additive term, $\sigma_\omega = B \cdot \omega / I_\omega$ (bimoment B multiplied by the sectorial coordinate $\omega$, divided by the sectorial moment of inertia $I_\omega$ directly analogous to the ordinary bending stress $\sigma = M \cdot y / I$), superimposed on the ordinary bending stress. In thin, open profiles precisely the sections for which restrained torsion effects are strongest this additional stress can represent a substantial fraction of the total, and neglecting it can lead to an unconservative assessment of member capacity.

The theoretical treatment of restrained (non-uniform) torsion in thin-walled bars originates with Timoshenko's formulation of the governing differential equation for the angle of twist of an open thin-walled member [2], and was subsequently developed into a complete and self-consistent theory of thin-walled bars encompassing bending, torsion and their coupling through the sectorial coordinate by Vlasov [3]. Bychkov [4] systematised this theory for practical structural analysis, providing extensive tabulated closed-form solutions for common structural schemes, and Gjelsvik [5] later gave an influential English-language synthesis of the underlying mechanics, still widely used as a reference text. This classical framework the fourth-order governing differential equation for the angle of twist θ(z) formulated by Vlasov [3], together with the sectorial geometric properties $\omega$, $I_\omega$ of the cross-section remains the theoretical basis of virtually all subsequent work on the subject, including the finite element and design-oriented contributions discussed below.

On the computational side, Friberg [6] was among the first to cast Vlasov's theory directly into a beam finite element with warping as an independent nodal degree of freedom, a formulation that underlies the element used in the present study and in much of the subsequent literature. Since then, the finite element treatment of restrained torsion has been extended considerably to include secondary (Saint-Venant) torsional moment deformation effects, boundary element formulations, and coupling with generalised beam theory (GBT) cross-section deformation modes [7] and a comprehensive state-of-the-art survey of GBT-based approaches to thin-walled member analysis, covering several hundred contributions, has recently been compiled by Mittelstedt [8, 22]. These developments, while considerably more general than the two-node element used here, share the same underlying differential relationship between bimoment and twist that underlies the two-node formulation used in this study.

Despite this long theoretical and computational pedigree, the practical calculation of the bimoment for a given loading and support condition remains a persistent difficulty in everyday structural design, and a number of steel design codes that require a bimoment check in their strength interaction formulas stop short of providing guidance on how B itself is to be obtained from the applied loading. One long-standing response to this difficulty is the bending–bimoment analogy: since the bimoment satisfies a differential relationship formally identical to that of the bending moment, an approximate bimoment diagram can often be inferred directly from the (much more familiar) bending moment diagram of the same member. This idea, applied to I-, C- and Z-sections, was developed into a practical design tool by Boothby [9], who additionally proposed a 'bimoment distribution' method an analogue of moment distribution for continuous members, and explicitly noted, using the parameter $L/a$ (equivalent to $k{\cdot}L$ in the present notation), that the accuracy of the direct analogy decreases as $L/a$ increases, tabulating correction factors over $L/a$ = 0.5–20 to extend the method beyond the range in which the direct analogy alone is reliable. This line of work was carried into mainstream American design practice through the AISC torsion design guide of Seaburg and Carter [10], which remains, decades later, a standard practitioner reference for torsional analysis of steel members, including tabulated torsional functions for the same classical support and loading cases considered here. Related bending-analogy formulations have since been proposed for other configurations, including beams with elastically restrained warping at the supports [11].

This body of work has not, however, closed the gap in current design practice. Aguero et al. [12], in a paper published in 2025, present a comprehensive treatment of the plastic and elastic resistance of Class 1–4 open sections under bimoment according to Eurocode 3, including two independently validated methods for locating the plastic shear centre and computing the plastic bimoment; however, their worked examples all take the bimoment as a given input to a cross-sectional check (e.g. B = 10,000 kN·cm²) rather than deriving it from a structural analysis, and their reference list does not engage with the bending-analogy or sectorial-coordinate literature discussed above.

Separately, a 2024 doctoral dissertation by Rybakov [13] addresses restrained torsion of light-gauge cold-formed steel members the design context most closely associated with the Direct Strength philosophy reviewed by Schafer [14] and codified in specifications such as [15]. It revisits the direct bending–bimoment analogy in an explicit tabulated form suited to routine design use, expressing the approximate bimoment as the bending moment scaled by the load eccentricity and by a correction factor dependent on member length and the flexural-torsional parameter. This

formulation is validated against nine classical loading/support schemes, with a maximum deviation from the exact solution of 4.6%. All nine validation cases, however, are evaluated for cold-formed sections with $k$ of order $10^{-4}$–$10^{-3}$ cm$^{-1}$, and the dissertation does not revisit or cite Boothby's finding that the direct analogy degrades as $k{\cdot}L$ grows, so the question of how the method performs outside this range is left open forty years after it was first raised. Independently, Polinkevich [16] working on the torsion of anisotropic thin-walled bars confirms, as a special case of a more general iterative method, that the classical Vlasov solution is recovered exactly, providing further independent corroboration of the theoretical baseline used in the present study.

The present study therefore does not claim to discover that the direct bending–bimoment analogy approximation degrades with increasing $k{\cdot}L$ a fact already known since 1984 but instead re-examines this known behaviour with four contributions not previously available together. First, the classical Vlasov closed-form solutions for four representative structural schemes are re-derived independently and verified both algebraically, by symbolic computation, and numerically, against a purpose-built two-node finite element formulated directly from the governing differential equation, in the spirit of [6] providing a verification toolchain that does not depend on commercial finite element software or on hand-interpolated tables. Second, it is shown, by direct numerical demonstration rather than by tabulation alone, that the relative error of the approximation is a universal, dimensionless function of $k{\cdot}L$, independent of section geometry, material, or load magnitude a general statement implicit in, but not made explicit by, Boothby's scheme-specific tables. Third, this universal relationship is used to test specifically the current (2024) tabulated formulation, showing that the same limitation identified in 1984 recurs in a formulation published forty years later without reference to it. Fourth, by evaluating the four schemes on both a hot-rolled and a cold-formed section, it is shown that the applicability boundary is scheme-dependent in particular, cantilever members already exceed a 5% tolerance within the cold-formed range that the direct analogy is otherwise considered safe for a sensitivity not identified in the earlier literature. The practical consequence of neglecting the bimoment altogether is then illustrated through a representative strength-interaction check set against the combined-stress provisions of several national design standards [17–19].

In summary, the novelty of this study is not a new theoretical formulation, the governing equation and its closed-form solutions for these schemes are classical [2,3], but a verification-oriented re-examination of an existing, widely used engineering approximation, combining independently re-derived closed-form solutions, an independent finite element check, and a general, scheme-resolved applicability chart not previously available in the literature. Restrained-torsion problems continue to attract renewed analytical attention elsewhere in the recent literature (e.g. the asymptotic-splitting treatment of open-section restrained torsion by Gorynin et al. [21]), underscoring that the underlying mechanics, though classical, remain an active subject of verification and re-derivation rather than a fully closed topic.

## METHODOLOGY

### Governing equation and general solution

For a prismatic thin-walled open-section member subjected to a distributed torque $m_t(z)$ about its longitudinal axis $z$, the angle of twist $\theta(z)$ satisfies the fourth-order differential equation established by Timoshenko [2] and cast into its now-standard form by Vlasov [3]:

$$EI\omega \cdot \theta^{(4)}(z) - GI_d \cdot \theta''(z) = m_t(z) \qquad (1)$$

where: $E$ and $G$ are the elastic and shear moduli, $I_\omega$ is the sectorial (warping) moment of inertia of the cross-section, and $I_d$ is the Saint-Venant torsion constant.

The bimoment and the total torque are related to $\theta(z)$ by:

$$\begin{aligned} B(z) &= -EI_\omega \cdot \theta''(z), \\ T(z) &= G \cdot I_d \cdot \theta'(z) - EI_\omega \cdot \theta'''(z) \end{aligned} \qquad (2)$$

and the resulting normal stress at a point of sectorial coordinate $\omega$ is $\sigma_\omega(z) = B(z){\cdot}\omega/I_\omega$, to be superimposed on the bending stress [3,5]. Introducing the flexural-torsional characteristic parameter:

$$k = \sqrt{\frac{G \cdot I_d}{EI_\omega}} \qquad (3)$$

the general solution of the homogeneous form of Equation 1 is $\theta_h(z) = C_1 + C_2 z + C_3 \cosh(kz) +$

$C_4 \sinh(kz)$; a particular solution is added for the specific form of $m_t(z)$, and the four constants are fixed by the boundary conditions at the two ends of the member. Two boundary conditions recur throughout this study – a fork (fork-type) support physically realised by restraining the flange tips against relative lateral movement while leaving them free to warp axially, which restrains the twist but leaves warping free ($\theta = 0$, $\theta'' = 0$, i.e. $B = 0$), and a fixed support, which restrains both twist and warping ($\theta = 0$, $\theta' = 0$). A free end, where no external torque or bimoment is applied, corresponds to the natural conditions $\theta'' = 0$ and $G \cdot I_d \theta' - EI_\omega \theta''' = 0$.

## Closed-form solutions for four representative schemes

Four structural schemes, chosen to span the classical combinations of support condition and load type, are considered throughout this study:

- Scheme A – simply supported member (fork supports at both ends), under a uniformly distributed transverse load $q$ applied with eccentricity e from the shear centre (equivalent to a uniformly distributed torque $m_t = q \cdot e$);
- Scheme B – fixed-fixed member, under the same eccentric distributed load;
- Scheme C – cantilever member (fixed at $z = 0$, free at $z = L$), under the same eccentric distributed load;
- Scheme D – simply supported member (fork supports), under a concentrated transverse load $P$ applied with eccentricity $e$ at mid-span (equivalent to a concentrated torque $T = P \cdot e$ at $z = L/2$).

Figure 1 illustrates the four schemes schematically: the support symbols follow the standard convention (a triangular, roller-type symbol for the fork support, which restrains $\theta$ but not warping; a hatched wall symbol for the fixed support, which restrains both $\theta$ and $\theta'$), the curved arrow denotes the eccentric torque generated by the transverse load acting at distance e from the shear centre, and x is measured from the left end (or from the fixed end, for Scheme C) in every case. The corresponding bimoment distributions, obtained by solving Equation 1 with the boundary conditions established – each re-derived independently by symbolic computation for the present study, and confirmed to agree exactly, at the level of machine precision, with the corresponding published solutions [9,13]. These four schemes were selected, rather than the full nine-scheme set later considered by Boothby [9], because they span the two structurally distinct sources of warping restraint that govern the applicability of the bending–bimoment analogy approximation: a single restrained end with the opposite end free (Scheme C), two restrained ends acting together (Schemes A and B, differing only in whether the end restraint is a fork or a fixed support), and a concentrated rather than distributed torque (Scheme D). We show analytically that the relative error of the approximation depends on the load pattern within a scheme only through $k \cdot L$, so the four cases considered establish the functional form of this dependence for both restraint configurations represented among Boothby's nine schemes; the remaining five are permutations of the same fork/fixed boundary conditions under different combinations of distributed and concentrated load and

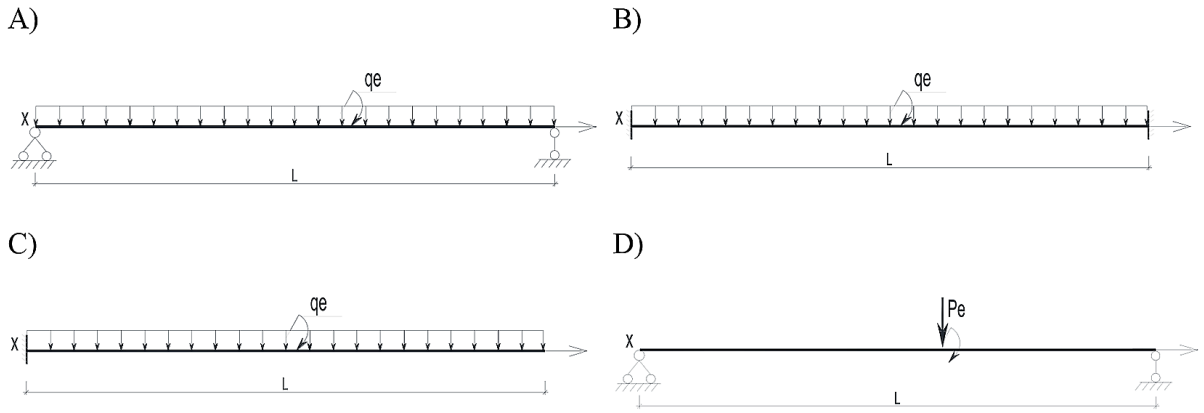



**Figure 1.** Structural schemes, all loaded eccentrically by e from the shear centre: (A) simply supported (fork supports), (B) fixed–fixed, and (C) cantilever (fixed–free), each under a uniformly distributed load $q$; (D) simply supported (fork supports) under a concentrated load $P$ at mid-span

are expected to interpolate between the trends already established here.

$$B_A(x) = (eq/k^2)\cdot[\sinh(kx)/\tanh(k\cdot L) - \cosh(kx) + 1 - \sinh(kx)/\sinh(k\cdot L)] \quad (4)$$

$$BB(x) = -eq[k^2L^2\cosh(kx) + k^2L^2\cosh(k(L-x)) - 2kL\sinh(kL) - 2kL\sinh(kx) - 2k\cdot L\sinh(k(L-x)) + 4\cosh(k\cdot L) - 4]/[2k^2(k\cdot L\sinh(kL) - 2\cosh(k\cdot L) + 2)] \quad (5)$$

$$B_C(x) = -eq[k\cdot L\sinh(k(L-x)) - \cosh(k\cdot L) + \cosh(kx)]/[k^2\cosh(k\cdot L)] \quad (6)$$

$$B_D(x) = (Pe/2k)\cdot\sinh(kx)/\cosh(k\cdot L/2),\ 0 \le x \le L/2 \text{ (symmetric about mid-span)} \quad (7)$$

with $x$ measured from the left support in each case. The corresponding bending moment diagrams, obtained by elementary statics, are:

$$M_A(x) = qx\cdot(L-x)/2,\quad M_B(x) = qx\cdot(L-x)/2 - qL^2/12,\quad M_C(x) = qLx - q\cdot(L^2+x^2)/2,\quad M_D(x) = Px/2\ (0 \le x \le L/2) \quad (8)$$

## The bending–bimoment analogy approximation

The similarity in form between Equations 4–7 and the corresponding entries in Equation 8 both being smooth functions of $x$ bounded by the same support conditions, and both vanishing (or attaining a stationary value) at the same points along the span is the basis of the bending–bimoment analogy approximation. Following Boothby [9], Seaburg and Carter [10] and, in a form adapted for routine tabulated design use, Rybakov [13], the bimoment is approximated as proportional to the bending moment at every section:

$$B^*(x) = M(x)\cdot e / (1 + \varphi) \quad (9)$$

where: $\varphi$ is a dimensionless constant, specific to the scheme and to the parameter $k\cdot L$, chosen so that Equation 9 reproduces the exact bimoment at the critical section $x_{cr}$ (the section of maximum $|B(x)|$):

$$\varphi = M(x_{cr})\cdot e / B(x_{cr}) - 1 \quad (10)$$

Equation 10 is mathematically equivalent to the scheme-specific closed-form expressions for $\varphi$(l, $k$) tabulated in [9,13], obtained there by direct algebraic manipulation of Equations 4–7; it is adopted here in this implicit form because it applies uniformly to any scheme without requiring a separate closed-form reduction, and because it is the form in which $\varphi$ is actually used in practice matched once at the critical (design) section. The accuracy of the approximation elsewhere along the span is then assessed through the relative error

$$\varepsilon(x) = [B^*(x) - B(x)] / |B(x_{cr})| \times 100\% \quad (11)$$

expressed, as in [9,13], as a percentage of the maximum bimoment rather than of the local value of $B(x)$, so that ε remains well defined at sections where $B(x)$ itself is small or changes sign. Because $M(x)$, $B(x)$ and $B^*(x)$ are all linear in the load magnitude and in the eccentricity $e$ for a given scheme and a given value of $k\cdot L$, Equation 11 depends on $x$, $L$ and $k$ only through the dimensionless combinations $x/L$ and $k\cdot L$ meaning that a single curve of $\varepsilon$ against $x/L$, computed once for a given $k\cdot L$, characterises the accuracy of the approximation for every section, material and load magnitude sharing that $k\cdot L$ value making it possible, once verified numerically, to construct a single scheme-resolved applicability chart valid for any open thin-walled section, rather than relying on discrete tabulated cases.

This normalisation has a direct consequence at sections where the local bimoment $B(x)$ is itself small: because $\varepsilon(x)$ is scaled by $|B(x_{cr})|$ rather than by $|B(x)|$, a given absolute discrepancy between $B^*(x)$ and $B(x)$ near a zero-crossing of $B(x)$ is reported as a correspondingly small percentage, whereas normalising by the (near-zero) local value would instead produce an arbitrarily large and practically uninformative percentage. This choice is conservative whenever the governing design check is controlled by the extreme value of the bimoment along the span, as is the case throughout Table 3 and Figure 6, since the local- and maximum-referenced error measures coincide exactly at that section. Away from the critical section, the maximum-referenced $\varepsilon(x)$ should be read as an error bound relative to the governing design value rather than as a measure of local relative accuracy; for the qualitative sign changes (Figure 5, Scheme C at high $k\cdot L$), direct visual comparison of $B(x)$ and $B^*(x)$ remains more informative than any single percentage.

## Weak form and element discretisation

To provide a verification tool independent of both the closed-form solutions derived earlier for the four schemes and of commercial finite element software, Equation 1 is discretised directly, following the general approach first used by Friberg [6] to cast Vlasov's theory into a warping-consistent beam element. Multiplying Equation 1 by an admissible virtual rotation $\delta\theta(z)$, integrating over an element of length $L_e$, and integrating the $EI_\omega$ term twice and the $I_d$ term once by parts gives the weak form:

$$\int_0^{L_e} EI_\omega \cdot \theta'' \delta\theta'' dz + \int_0^{L_e} GI_d \cdot \theta' \delta\theta' dz = \\ = \int_0^{L_e} m_t \cdot \delta\theta dz + [T \cdot \delta\theta - B\delta\theta']\Big|_0^{L_e} \quad (12)$$

which requires $\theta$ to be interpolated with $C^1$ continuity. A two-node element is used, with two degrees of freedom per node the twist $\theta$ and its derivative $\theta'$ interpolated by the standard cubic Hermite shape functions $N_1 \ldots N_4$, identical in form to those used for the transverse displacement of an Euler–Bernoulli beam element:

$$\theta(s) = N_1(s)\theta_1 + N_2(s) \\ \theta_1' + N_3(s)\theta_2 + N_4(s)\theta_2', \; 0 \le s \le L_e \quad (13)$$

It is worth clarifying explicitly what "two-node" refers to here, since finite elements for thin-walled members are often described instead by their number of degrees of freedom (DOF) per node. The two nodes are the two end cross-sections of the element along the member axis z exactly as for any standard 1-D bar or beam element and are unrelated to the number of DOF carried at each node. The element used here carries only two DOF per node, $\theta$ and $\theta'$, because Equation 1 is a scalar equation in the single unknown $\theta(z)$: the four schemes treat torsion as an independent sub-problem, with the bending moment M(x) obtained separately from statics (Equation 8) and combined with $B(x)$ only afterwards, in the stress superposition performed later in the combined strength check. This is deliberately more restrictive than the general spatial beam elements used elsewhere in the literature for fully coupled bending–torsion analysis, which typically carry additional translational and rotational DOF per node for example the seven-DOF formulation used in [13], or the warping-augmented Timoshenko elements reviewed in [7] and which would be the appropriate choice if bending and torsion needed to be solved simultaneously rather than superposed. The present two-node, four-DOF-per-element formulation is the minimal one consistent with Equation 1 alone, which is all that is required to verify the closed-form solutions derived earlier for the four support/loading schemes. Essential (Dirichlet) boundary conditions are imposed by constraining the $\theta$ degree of freedom (fork support) or both the $\theta$ and $\theta'$ degrees of freedom (fixed support) at the relevant node; a free end requires no constraint, the natural conditions of the governing differential equation being satisfied automatically by the variational formulation.

## Element stiffness matrix and load vector

Substituting Equation 13 into the two integrals of Equation 12 gives the element stiffness matrix as the sum of two 4 × 4 matrices:

$$K_e = K_b + K_g \quad (14)$$

where: $K_b$, arising from the $EI_\omega \cdot \theta'' \cdot \delta\theta''$ term, is formally identical to the standard Euler–Bernoulli bending stiffness matrix with $EI_\omega$ in place of EI:

$$K_b = \left(\frac{EI_\omega}{L_e^3}\right) \cdot \begin{bmatrix} 12 & 6L_e & -12 & 6L_e \\ 6L_e & 4L_e^2 & -6L_e & 2L_e^2 \\ -12 & -6L_e & 12 & -6L_e \\ 6L_e & 2L_e^2 & -6L_e & 4L_e^2 \end{bmatrix} \quad (15)$$

and $K_g$, arising from the $I_d\,\theta' \cdot \delta\theta'$ term, is formally identical to the classical geometric (stability) stiffness matrix of a beam-column under axial tension $N = GI_d$, in the standard form given e.g. by Przemieniecki [20], as a consequence of the differential Equation 1 being, term for term, the equilibrium equation of a beam-column with tensile axial force $I_d$ in place of $N$:

$$K_g = \left(\frac{GI_d}{30L_e}\right) \cdot \begin{bmatrix} 36 & 3L_e & -36 & 3L_e \\ 3L_e & 4L_e^2 & -3L_e & -L_e^2 \\ -36 & -3L_e & 36 & -3L_e \\ 3L_e & -L_e^2 & -3L_e & 4L_e^2 \end{bmatrix} \quad (16)$$

It should be emphasised that the term "geometric stiffness matrix" for $K_g$ reflects only a

mathematical correspondence, inherited from the beam-column literature, and not a second-order or stability effect: Equation 1 is a linear equation with a real physical coefficient, $GI_d$, the Saint-Venant torsional stiffness of the cross-section, multiplying $\theta''$. There is no axial force, no $P$–$\Delta$ effect, and no geometric nonlinearity anywhere in the present formulation. The correspondence arises purely because the beam-column equilibrium equation $EI \cdot v'''' - N \cdot v'' = q$, in which $N$ is a compressive (or, with a sign change, tensile) axial force, is term-for-term identical to Equation 1 with $EI \leftrightarrow EI_\omega$, $v \leftrightarrow \theta$ and $N \leftrightarrow GI_d$; $K_g$ is therefore obtained from the same integral, $\int GI_d\, \theta'\delta\theta'\, dz$ in place of $\int Nv'\delta v'dz$, and happens to take the algebraic form long tabulated for beam-column elements under axial tension. The label is retained here only because it is the term most readily recognised by readers familiar with standard finite element texts; no stability interpretation should be attached to it.

For an element subjected to a uniformly distributed torque $m_0 = q \cdot e$, the consistent nodal load vector, obtained from the right-hand side of Equation 12, is

$$\mathrm{f_e} = \mathrm{m_0} \cdot \left[ \frac{\mathrm{L_e}}{2} \quad \frac{\mathrm{L_e^2}}{12} \quad \frac{\mathrm{L_e}}{2} \quad \frac{-\mathrm{L_e^2}}{12} \right]^{\mathrm{T}} \qquad (17)$$

A concentrated torque $T$ applied at a node (Scheme D) is introduced directly as a nodal force conjugate to the corresponding $\theta$ degree of freedom. Global matrices are assembled from Equations 14 and 17 in the usual direct-stiffness manner, and the bimoment is recovered at any point within an element from the second derivatives of the shape functions, $B(s) = -EI_\omega \theta''(s)$, consistent with Equation 2.

## Verification

The element formulated from the weak form and stiffness matrices derived above was implemented independently in Python and in MATLAB and used to solve Scheme A, the simply supported (fork-fork) member under uniformly distributed load for the UPN200 (Section H) reference case study, $L = 400$ cm (Table 1).

The solution converges monotonically to the exact value, at the rate expected of a conforming cubic-Hermite discretisation of a fourth-order self-adjoint problem, providing confidence that the element formulation and its implementation are correct. To confirm that this agreement is not specific to Scheme A, the same element (64 elements per member) was assembled and solved independently for all four support/loading schemes, using the reference properties of Section H at $L = 400$ cm. Table 2 compares the resulting critical bimoment against the exact closed-form value at the same section.

**Table 1.** Convergence of the finite element solution (Scheme A, UPN200 Section H reference case, $L$ = 400 cm)

| Elements | B at mid-span (kN.cm²) | Error relative to Equation 4 |
|---|---|---|
| 2 | 371.19 | 16.83% |
| 4 | 323.38 | 1.78% |
| 8 | 318.80 | 0.34% |
| 16 | 317.97 | 0.08% |
| 32 | 317.78 | 0.02% |
| 64 | 317.73 | 0.005% |

The finite element result agrees with the exact solution to within 0.2% for every scheme at this mesh density, confirming that the element formulation described above together with its implementation of the fork, fixed, and free-end boundary conditions defined earlier, including the natural conditions of the cantilever scheme is correct in general, not only for the single scheme used in the convergence study above. This element, rather than the closed-form solutions for the four schemes (which are exact but scheme-specific), is the tool subsequently used to confirm, for a small but representative number of spot checks, that the parametric sweep obtained analytically is not an artefact of the closed-form derivation.

The 64-element mesh used for Table 2, and for every finite-element spot check reported subsequently in this study, was selected directly from the convergence data of Table 1 – doubling the mesh from 32 to 64 elements changes the computed critical bimoment by only 0.015 percentage points (from 0.02% to 0.005% relative error), well below the level at which discretisation error could influence any conclusion drawn from the parametric study, which in any case relies primarily on the closed-form solutions rather than on the finite element itself. Since Table 2 confirms agreement with the exact solution to within 0.2% across all four schemes at

**Table 2.** Finite element validation across all four schemes (Section H, L = 400 cm, 64 elements)

| Scheme | $B_{cr}$, FEM (kN·cm²) | $B_{cr}$, exact (kN·cm²) | Difference |
|---|---|---|---|
| A - simply supported | 317.73 | 317.71 | 0.005% |
| B - fixed-fixed | −994.47 | −996.13 | 0.17% |
| C - cantilever | −2316.98 | −2320.3 | 0.14% |
| D - point load, mid-span | 1322.30 | 1323.96 | 0.13% |

this density, the same 64-element mesh is used without further mesh-sensitivity study for every subsequent finite-element check in this paper, and discretisation error is judged negligible relative to the other sources of approximation.

## NUMERICAL EXAMPLE

### Section geometry and properties

Two channel sections, chosen to represent the two ends of the range of flexural-torsional stiffness ratio $k$ encountered in practice, are used throughout the remainder of this study.

The first, denoted Section H (hot-rolled), is a European standard UPN200 channel ($h$ = 200 mm, $b$ = 75 mm, $t_f$ = 11.5 mm, $t_w$ = 8.5 mm, per EN 10365), computed here using an idealised uniform-thickness thin-wall centreline model consistent with the classical Vlasov-type thin-walled bar theory used throughout this study. This idealisation gives $A$ = 32.3 cm², $I_x$ = 1920 cm⁴, $I_y$ = 169 cm⁴, $I_d$ = 11.0 cm⁴, $I_\omega$ = 10,500 cm⁶, and a shear-centre offset from the centroid of 44.5 mm. Comparison with the manufacturer's catalogue values for the same nominal section ($I_x$ = 1910 cm⁴, $I_d$ = 11.9 cm⁴, $I_\omega$ = 9070 cm⁶, shear-centre offset 39.4 mm) shows differences of 0.5% for $I_x$ but 7–16% for the torsion-related quantities $I_d$, $I_\omega$ and the shear-centre location. This systematic deviation is expected and well understood: catalogue values are computed for the true rolled geometry, including the taper of the flanges and the fillets at the flange-web junctions, neither of which is represented in the uniform-thickness centreline idealisation of classical thin-walled bar theory. The idealisation is nonetheless retained here, consistent with the classical thin-walled beam theory outlined earlier, and is the same idealisation implicit in any finite-element model that represents the member by its centreline geometry.

The second, denoted Section C (cold-formed), is a plain (unlipped) channel of overall dimensions 100 × 200 × 2 mm, broadly representative of the light-gauge members covered by cold-formed steel design specifications such as [15] and by the direct strength design philosophy reviewed in [14] (Figure 2). It is chosen to match the overall size of the profile used as a worked example in [13] (there termed a "stud profile"), though without the edge lips present in that profile, a difference noted explicitly here so that the present results are not mistaken for a reproduction of the lipped-profile values reported there. For this section, the same idealised thin-wall procedure gives $I_d$ = 0.106 cm⁴ and $I_\omega$ = 5550 cm⁶.

With $E$ = 210 GPa, $G$ = E/2.6 for Section H, and $E$ = 206 GPa, $G$ = 80 GPa (as used in [13]) for Section C, the flexural-torsional parameters (Eq. 3) are $k_H$ = 0.0201 cm⁻¹ and $k_C$ = 0.00272 cm⁻¹, confirming, as expected from the cubic dependence of $I_d$ on wall thickness, that Section C's parameter is smaller than Section H's by a factor of approximately 7.4. Figure 3 shows the two cross-sections together with their normalised sectorial coordinate $\omega_n$, and the location of the centroid G and shear centre SC, the latter lying, in both cases, outside the profile on the side opposite the flanges, as is characteristic of channel sections.

For each section, the transverse load is taken to act in the plane of the web, a common situation in practice (e.g. a purlin loaded through a roof sheet fastened along the web line, or a beam supporting a wall bracket at the web); the resulting eccentricity relative to the shear centre is $e_H$ = 2.66 cm and $e_C$ = 6.19 cm respectively.

The independence of the applicability chart from cross-sectional shape follows directly from Equation 11, which does not reference section geometry except through the scalar $k$; this is confirmed here for two further open sections beyond the channels considered above, computed with the same tree-structured

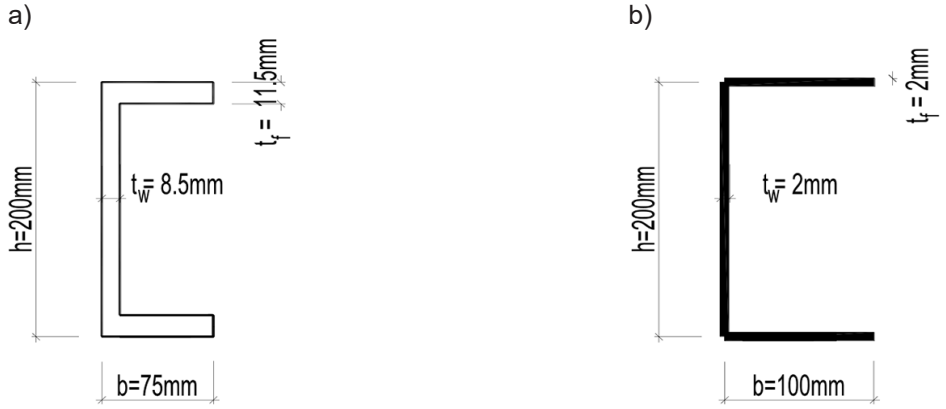



**Figure 2.** Cross-sectional dimensions of the two reference members: (a) Section H – hot-rolled UPN200 channel (EN 10365); (b) Section C – cold-formed plain channel (100 × 200 × 2 mm)

sectorial-coordinate procedure used throughout. An unequal-flange I-section ($b_u$ = 100 mm, $b_l$ = 60 mm, $h$ = 187 mm, $t_f$ = 13 mm, $t_w$ = 10 mm, after [12]) gives $I_d$ = 16.05 cm⁴, $I_\omega$ = 3500 cm⁶, $k$ = 0.0339 cm⁻¹; a lipped cold-formed channel ($h$ = 200 mm, $b$ = 100 mm, lip $c$ = 20 mm, $t$ = 2 mm) gives $I_d$ = 0.116 cm⁴, $I_\omega$ = 9338 cm⁶, $k$ = 0.00223 cm⁻¹. Both $k$ values fall within the same order of magnitude as, and bracket, the two channels studied in detail below ($k_H$ = 0.0201 cm⁻¹, $k_C$ = 0.00272 cm⁻¹), and both were obtained from a branching (I-section) or five-segment (lipped channel) idealisation of the same algorithm used for the three-segment plain channel, confirming that the sectorial-coordinate procedure is not restricted to the simplest open-section topology. Because $\varepsilon(\xi; k{\cdot}L)$ itself is, by construction, a function of $k{\cdot}L$ alone, evaluating it for either section at any $k{\cdot}L$ already tabulated in Table 4 reproduces the same error profile to within floating-point precision; the substantive numerical content of the applicability chart (Figure 6, Table 5) therefore extends unchanged to any open thin-walled cross-section for which the sectorial coordinate can be computed, including the I-section and lipped channel confirmed numerically here, and, by the same tree-structured algorithm applied to a different open-chain or branching topology, Z-sections, hat sections and other common cold-formed profiles, whose torsional and flexural-torsional behaviour continues to be studied experimentally and numerically in the recent literature [23].

## Structural schemes and reference spans and results

The four schemes described earlier (Schemes A–D) are evaluated for Section H at a span of $L$ = 400 cm representative of a hot-rolled channel used as a beam or purlin and for Section C at spans of $L$ = 400 cm and $L$ = 600 cm, spanning the typical range of cold-formed purlin spacing. The corresponding values of the dimensionless parameter $k{\cdot}L$ are: Section H at $L$ = 400 cm, $k{\cdot}L$ = 8.04; Section C at $L$ = 400 cm, $k{\cdot}L$ = 1.09; Section C at $L$ = 600 cm, $k{\cdot}L$ = 1.63 placing Section H well beyond, and Section C within or at the edge of, the range ($k{\cdot}L$ corresponding to $k \sim 10^{-4}$–$10^{-3}$ cm⁻¹ and $l$ = 1–6 m) for which the bending–bimoment analogy approximation was validated in [13]. Figure 4 shows the exact bimoment distribution $B(x)$, Equations 4–7, for Section H over the four schemes. The distributions differ markedly in shape the fixed-fixed and cantilever schemes (B, C) show their extreme values at the supports, the simply-supported schemes (A, D) at mid-span but all four are computed from the same section properties and the same closed-form theory.

Table 3 summarises, for each section/span combination and each scheme, the exact critical bimoment $B(xcr)$ and the maximum error of the bending–bimoment analogy approximation, Eq. (11), over the full span.

For Section H, the bending–bimoment analogy approximation exceeds a 5% tolerance by a wide margin in all four schemes, reaching over 55% for the cantilever scheme. For Section C, at both spans, three of the four schemes (A, B, D) remain within, or close to, the 5% tolerance

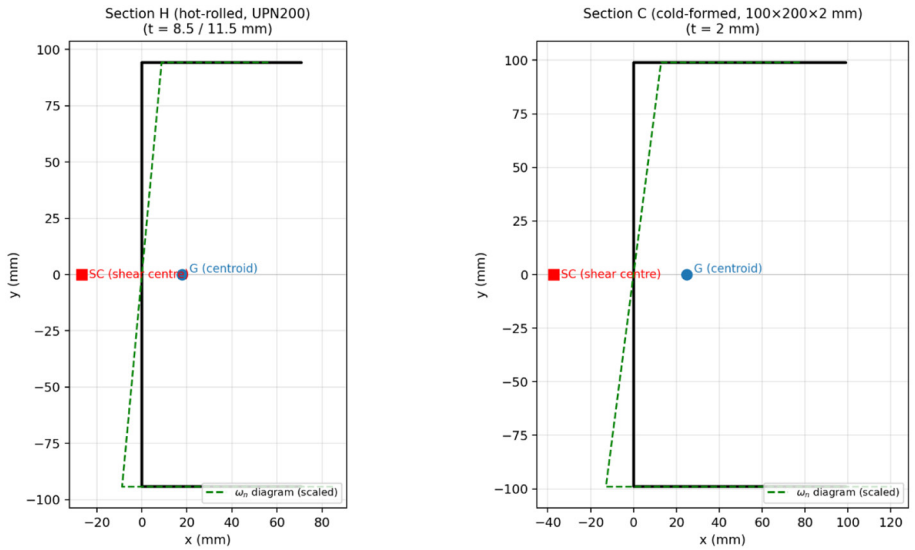



**Figure 3.** Cross-section geometry, sectorial coordinate diagram ($\omega_n$), centroid (G) and shear centre (SC) for Section H (UPN200) and Section C (100 × 200 × 2 mm)

generally considered acceptable for this type of engineering approximation, consistent with the validation range reported in [13] but the cantilever scheme (C) already exceeds this tolerance at both spans, including at the shorter, 400 cm span. This scheme-dependence, and its consequences for the applicability of the approximation in general, is examined systematically in the parametric study that follows.

The magnitude entries in Table 3 summarise the error at a single (critical) section; Figure 5 makes the comparison visual and shows the full distribution. It plots the exact bimoment $B(x)$, Equation 4/6, together with the bending–bimoment analogy approximation $B^*(x)$, Equation 9, for Scheme A and Scheme C, at a low $k{\cdot}L$ case (Section C, $L$ = 600 cm, $k{\cdot}L$ = 1.63) and a high-$k{\cdot}L$ case (Section H, $k{\cdot}L$ = 8.04).

At $k{\cdot}L$ = 1.63 (bottom row), the two curves are visually indistinguishable for Scheme A and differ only modestly for Scheme C. At $k{\cdot}L$ = 8.04 (top row), the approximation for Scheme

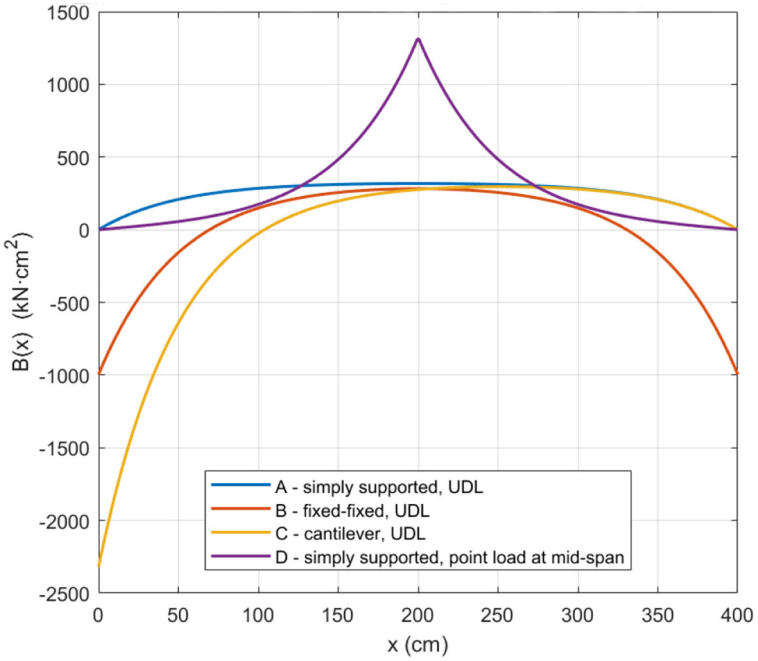



**Figure 4.** Exact bimoment distribution B(x) for Section H, Schemes A–D, $L$ = 400 cm

**Table 3.** Critical bimoment and maximum error of the bending–bimoment analogy approximation (loads: Section H – q = 0.05 kN/cm, P = 20 kN; Section C – q = 0.005 kN/cm, P = 2 kN)

| Section | Span | k·L | Scheme | $B(x_{cr})$ (kN·cm²) | max \|ε(x)\| |
|---|---|---|---|---|---|
| H | 400 cm | 8.04 | A – simply supported | 317.7 | 21.9% |
| H | 400 cm | 8.04 | B – fixed–fixed | −996.1 | 21.7% |
| H | 400 cm | 8.04 | C – cantilever | −2320.3 | 55.5% |
| H | 400 cm | 8.04 | D – point load, mid–span | 1324.0 | 40.6% |
| C | 400 cm | 1.09 | A – simply supported | 550.74 | 0.6% |
| C | 400 cm | 1.09 | B – fixed-fixed | −404.62 | 0.7% |
| C | 400 cm | 1.09 | C – cantilever | −1971.29 | 9.7% |
| C | 400 cm | 1.09 | D – point load, mid-span | 1128.50 | 1.8% |
| C | 600 cm | 1.63 | A – simply supported | 1088.57 | 1.4% |
| C | 600 cm | 1.63 | B – fixed-fixed | −889.48 | 1.6% |
| C | 600 cm | 1.63 | C – cantilever | −3716.33 | 17.7% |
| C | 600 cm | 1.63 | D – point load, mid-span | 1531.02 | 4.0% |

A is visibly flatter than the exact curve near the supports, and for Scheme C it is qualitatively as well as quantitatively wrong over most of the span, the exact solution changes sign around $x \approx 100$ cm, a feature the bending–bimoment analogy curve, constrained to be proportional to the single-signed bending-moment diagram $M_C(x)$ of Equation 8, cannot reproduce at all. This qualitative failure, rather than only the quantitative error already tabulated in Table 3, is the clearest illustration of why the approximation should not be extrapolated beyond the $k{\cdot}L$ range established by the parametric study above.

## Applicability range of the bending–bimoment analogy

### *The error is a universal function of k·L*

Equation 11 already indicates why the relative error of the bending–bimoment analogy approximation should depend on $x$, $L$ and $k$ only through the dimensionless combinations $x/L$ and $k{\cdot}L$, rather than on $x$, $L$ and $k$ separately. This can be seen directly from the structure of Equations 4–10. Introducing the dimensionless coordinate $\xi = x/L$ and the dimensionless group $\eta = k{\cdot}L$, each of the closed-form bimoment expressions (4)–(7) can be written, after factoring out the load and eccentricity, in the form $B(\xi,\eta) = (e{\cdot}Q{\cdot}L^2)\cdot b(\xi,\eta)$, where Q denotes the load parameter ($Q = q$ for Schemes A–C, Q = P for Scheme D) and $b$ is a dimensionless function; likewise each bending-moment expression (8) can be written $M(\xi) = (Q{\cdot}L^2)\cdot m(\xi)$. Because $e$ and the load magnitude multiply both $B$ and $M$ in the same way, they cancel identically in the ratio that defines $\varphi$ (Equation 10) and in the error $\varepsilon$ (Equation 11), leaving both $\varphi$ and $\varepsilon$ as functions of $\eta = k{\cdot}L$ alone ($\varphi$) or of $\xi$ and $\eta$ alone ($\varepsilon$), independent of $e$, of the load magnitude, and since $I_\omega$ and $I_d$ enter $B(x)$ only through $k$ independent of the section's absolute geometric properties or material constants individually. Only the single combination $k{\cdot}L$ controls the shape and magnitude of the error.

This is confirmed numerically, to a precision limited only by floating-point round-off, by evaluating ε(x) for two sections with entirely different $k$, load and span but the same product $k{\cdot}L$. Table 4 compares the error profile for Section H-like properties ($k = 0.02$ cm$^{-1}$, $L = 100$ cm, giving $k{\cdot}L = 2.00$) against a section with $k = 0.00272$ cm$^{-1}$ and $L = 735.6$ cm (giving the same $k{\cdot}L = 2.00$, but with $k$ about seven times smaller and $L$ about seven times larger), for Scheme A.

The two profiles agree to within $2 \times 10^{-4}$ percentage points at every station, that is, to the level of numerical precision of the calculation, not merely approximately. The same agreement is obtained for Schemes B, C and D, and for other pairs of ($k$, $L$) combinations giving the same $k{\cdot}L$. This confirms, by direct numerical demonstration rather than by inference from tabulated cases, that a single curve $\varepsilon(\xi; k{\cdot}L)$ or, more usefully for design, a single curve of max|ε| versus $k{\cdot}L$ fully characterises the accuracy of the bending–bimoment analogy approximation for a given scheme, for any open thin-walled section, material and load magnitude.

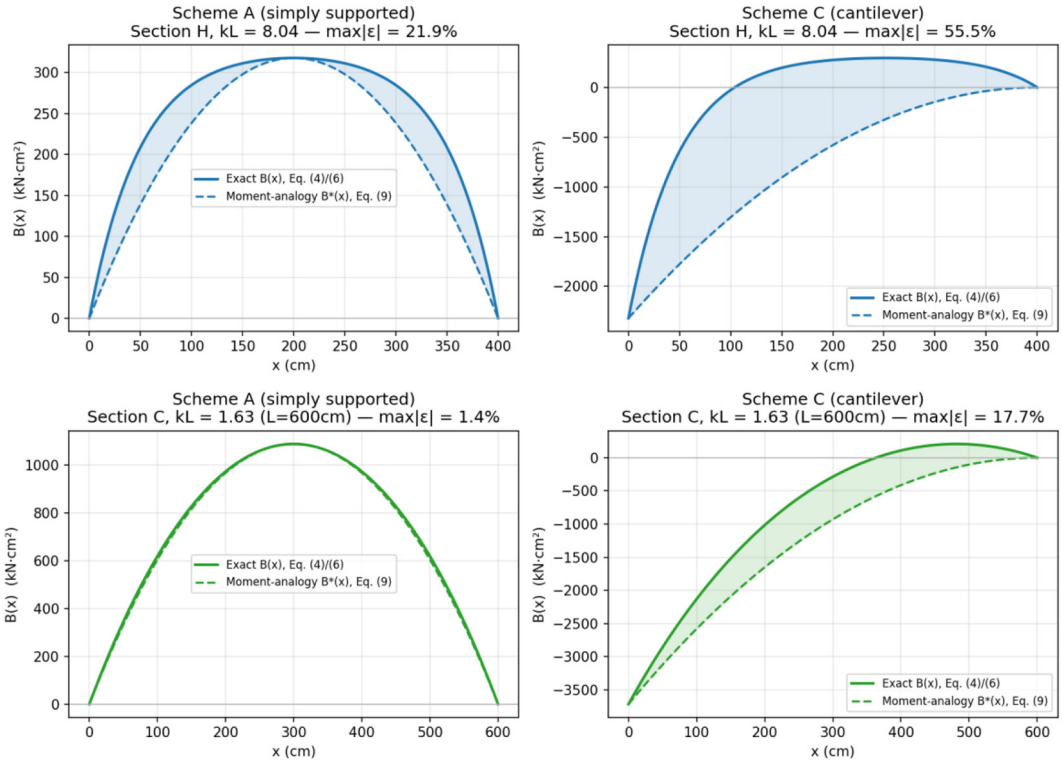



**Figure 5.** Exact vs. bending–bimoment analogy approximation of the bimoment distribution for representative low- and high $k \cdot L$ cases (Schemes A and C)

### *Applicability chart*

Figure 6 plots $\max|\varepsilon(x)|$ against $k \cdot L$, computed from the closed-form solutions for the four support/loading schemes over the continuous range $k \cdot L$ = 0–10, for all four schemes. The curve for each scheme is monotonically increasing, consistent with Boothby's original observation [9] that the direct analogy degrades as the flexural-torsional parameter grows, but the rate of degradation is markedly scheme-dependent. Solving $\max|\varepsilon(k \cdot L)| = 5\%$ numerically for each scheme gives the following applicability limits (Table 5).

The ordering is consistent with the case-study results for the two reference sections presented earlier: Section C at $k \cdot L$ = 1.09–1.63 lies safely below the limit for Schemes A, B and D, but above the limit for Scheme C, explaining why the cantilever result of Table 3 (9.7–17.7%) already exceeds tolerance while the other three schemes (0.6–4.0%) do not. Section H, at $k \cdot L$ = 8.04, lies far beyond the applicability limit of all four schemes.

## Physical interpretation and recommended limits

The scheme-dependence of the applicability limit can be understood qualitatively from the boundary conditions involved. A cantilever provides only a single warping-restraining condition, at the fixed end; as $k \cdot L$ grows, the influence of this single restraint decays over an increasingly short fraction of the span (the characteristic decay length of the homogeneous solution is of order $1/k$), so that over most of a long cantilever the twist behaves as if unrestrained, a regime the bending–bimoment analogy built around the restrained solution does not represent well. A fixed-fixed or simply-supported member, by contrast, has warping-related conditions enforced at

**Table 4.** Universality of $\varepsilon(\xi; kL)$ – Scheme A, $k \cdot L$ = 2.00, two unrelated sections

| $\xi = x/L$ | 0 | 0.125 | 0.25 | 0.375 | 0.5 | 0.625 | 0.75 | 0.875 | 1 |
|---|---|---|---|---|---|---|---|---|---|
| $\varepsilon$, section 1 (%) | 0.000 | −1.989 | −1.500 | −0.466 | 0.000 | −0.466 | −1.500 | −1.989 | 0.000 |
| ε, section 2 (%) | 0.000 | −1.989 | −1.500 | −0.466 | 0.000 | −0.466 | −1.500 | −1.989 | 0.000 |

both ends, and the two boundary-layer regions interact more favourably with the shape of the bending-moment diagram, giving a slower degradation of the analogy.

Because the applicability limit is scheme-dependent and, for the cantilever case, occurs at a value of $k{\cdot}L$ (≈0.7) within or near the upper end of well within the range $k \sim 10^{-4}$–$10^{-3}$ cm$^{-1}$, $l$ = 1–6 m reported as validated for cold-formed sections in [13], a blanket statement that the bending–bimoment analogy is "safe for cold-formed steel" cannot be sustained without qualification by scheme. On the basis of Figure 6 and Table 5, it is recommended that the direct bending–bimoment analogy approximation, Equation 9, be restricted to $k{\cdot}L \lesssim 0.7$ for cantilever members, and to $k{\cdot}L \lesssim 1.8$–$3.2$ for the other three schemes considered, with the corrected or distribution-method formulations of [9,10] or a direct solution of Equation 1, for which the beam-type finite element formulation developed above provides a convenient tool used beyond these limits.

A natural question is whether a single generalised parameter, combining $k{\cdot}L$ with some measure of the degree of warping restraint at each end, could replace the four scheme-specific limits of Table 5 with one unified criterion. The physical interpretation above suggests why this is not straightforward: the cantilever scheme derives its low limit from having only one restrained end, so that a single boundary layer of width ~$1/k$ must, by itself, carry the entire departure from the unrestrained solution assumed implicitly by the analogy; the two-restrained-end schemes instead share this departure between two boundary layers that interact constructively with the shape of the bending-moment diagram. A one-parameter measure of restraint (for example, an effective-length factor analogous to those used in flexural buckling, the warping-stiffness-weighted parameters explored in recent torsion-aware cross-sectional optimisation studies [24], or a spring-stiffness formulation of the kind recently used to approximate simultaneous elastic restraint against warping and rotation at beam supports in lateral-torsional buckling [25]) would need to capture not only how many ends are restrained but the qualitatively different way in which one- and two-boundary-layer solutions decay along the span; the evidence above indicates that at least this coarse classification, one restrained end versus two is necessary, and a fully unified single parameter is left as a direction for future work.

**Table 5.** $k{\cdot}L$ beyond which the bending–bimoment analogy approximation exceeds a 5% tolerance

| Scheme | $k{\cdot}L$ (5% limit) |
|---|---|
| C – cantilever, UDL | 0.74 |
| D – simply supported, point load at mid-span | 1.84 |
| B – fixed-fixed, UDL | 2.99 |
| A – simply supported, UDL | 3.23 |

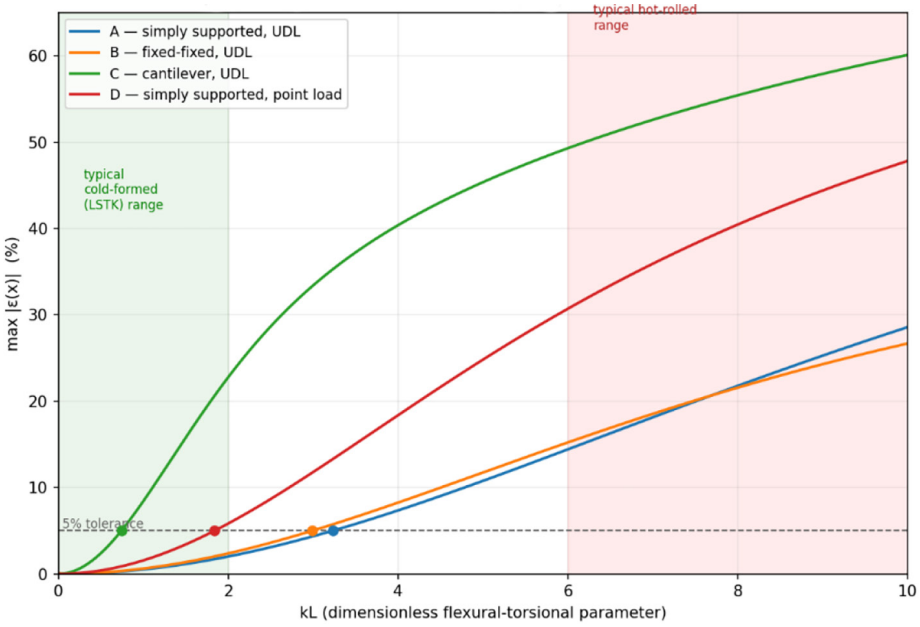



**Figure 6.** Applicability chart: max|ε| versus $k{\cdot}L$ for Schemes A–D

## Practical consequence: Combined strength check

### *Combined interaction check*

Once $B(z)$ is known whether from the exact solution of Equation 1, from the beam-type finite element formulation, or, within the applicability limits established by the parametric study above, from the bending–bimoment analogy approximation the associated normal (warping) stress is superimposed on the ordinary bending stress at every point of the cross-section:

$$\sigma(y,\omega) = M_x(z)\cdot y/I_{xn} \pm B(z)\cdot\omega/I_{\omega} \qquad (18)$$

with the sign of each term following the sign convention of the corresponding internal force and of $y$, $\omega$ at the point considered. Several national and regional steel design standards express the resulting strength requirement as a normalised interaction check of the form

$$|M_x\cdot y/I_{xn}| / (f_{yd}/\gamma_c) + |B\cdot\omega/I_{\omega}| / (f_{yd}/\gamma_c) \le 1 \qquad (19)$$

this is, for instance, essentially the form of the combined bending and bimoment check in the Vietnamese steel design standard TCVN 5575:2024 [17] (its Equation 42, for members without axial force), which follows closely the corresponding provision of the Russian standard SP 16.13330.2017 [18] on which it is historically based; the same physical superposition of bending and warping normal stresses also underlies the elastic cross-sectional checks of Eurocode 3 [19], discussed in the bimoment-resistance context by Aguero et al. [12]. Equation 19 is used here only as a representative, illustrative format common to this family of codes; the point made below concerns the physical superposition of Equation 18, not the particular normalisation of any one of them.

### *Reference case*

The check is illustrated for the same reference case already used for the finite element verification of Tables 1–2 and appearing in Table 3: Section H (the hot-rolled UPN200 channel introduced earlier), Scheme A, $q$ = 0.05 kN/cm, $L$ = 400 cm. At the critical section ($x = L/2$), this load gives a bending moment $M_x = 0.5\cdot q\cdot x\cdot(L-x)$ = 1000 kN·cm and, from Equation 4, the corresponding bimoment $B$ = 317.7 kN·cm² (consistent with Table 3); the two are not independently assumed but are the exact ($M_x$, $B$) pair produced by the same applied load. The bending stress is evaluated at the extreme fibre, $y = \pm 10$ cm (half the section depth), and the warping stress at four points spanning the cross-section: the outer tips and the flange-web junctions of both flanges (points A–D, Figure 7).

### *Results*

Table 6 and Figure 7 give the bending stress, the warping (bimoment) stress, and their sum at each of the four points.

At the flange-web junctions (B, C), the warping stress is opposite in sign to the bending stress and reduces the total by 14.6% relative to bending alone at these points, neglecting B is conservative. At the outer flange tips (A, D) where |ω| is largest, and which are, for this section and load case, also the points of maximum bending stress, the warping stress adds directly to the bending stress, increasing the total by 24.2%. Because the outer tips already govern under bending alone, they remain governing under the combined check, and the 24.2% increase there is the one that controls member capacity.

For additional verification at the free flange tips, the same reference case was also checked against an independent three-dimensional shell finite element model (Figure 8); the resulting flange-tip stress distribution along the span is compared with the closed-form prediction in Figure 9, and the results and their implications are discussed further below.

### *Consequence for design*

Since both $M_x$ and B are proportional to the same applied load for a given scheme and geometry (Equation 4 and Equation 8 are both linear in $q$), the ratio of total stress to bending-only stress at the governing point, 6.47/5.21 = 1.242, is independent of the particular yield criterion $f_{yd}/\gamma_c$ adopted in Equation 19: a design that checks only the bending term of Equation 19, implicitly assuming $B = 0$ will judge the member adequate at a load level 24.2% higher than the level at which the actual combined stress reaches the same limit. This is not a statement about the accuracy of the bending–bimoment analogy approximation examined earlier; it is a more basic observation that omitting the bimoment term from the strength check altogether, as is possible whenever a code requires the check but does not mandate

**Table 6.** Combined normal stress at the critical section (Section H, Scheme A, $L$ = 400 cm)

| Point | Location | $\sigma_{bend}$ (kN/cm²) | $\sigma_{bimo}$ (kN/cm²) | $\sigma_{total}$ (kN/cm²) | Change vs. bending alone |
|---|---|---|---|---|---|
| A | Bottom flange, outer tip | −5.21 | −1.26 | −6.47 | +24.2% |
| B | Bottom flange, web junction | −5.21 | +0.76 | −4.45 | −14.6% |
| C | Top flange, web junction | +5.21 | −0.76 | +4.45 | −14.6% |
| D | Top flange, outer tip | +5.21 | +1.26 | +6.47 | +24.2% |

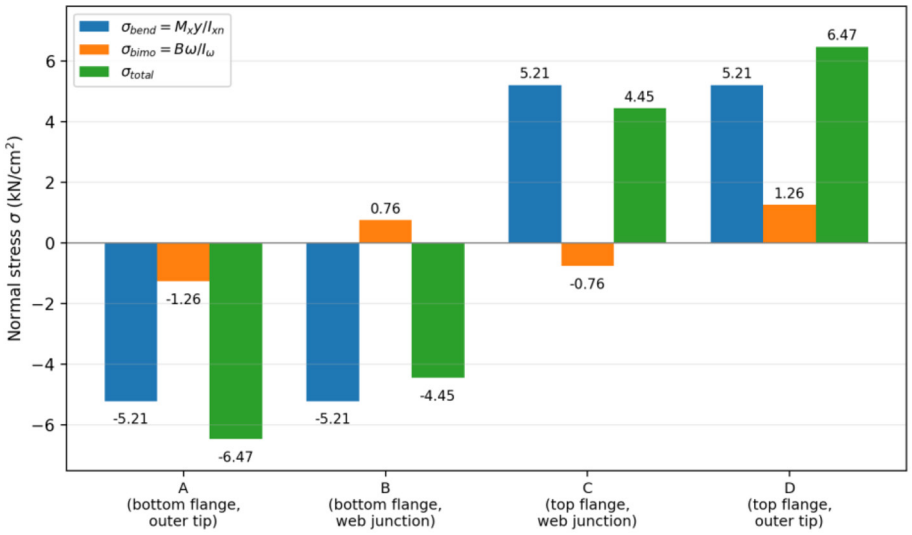



**Figure 7.** Combined normal stress (bending, warping, total) at four cross-sectional points

how $B$ is obtained, leads directly to an unconservative result at exactly the points (open flange tips) where thin-walled open sections are most vulnerable to warping stresses in the first place. The 24.2% figure above is specific to Scheme A at $k{\cdot}L = 8.04$; because both $M_x$ and $B$ scale linearly with the applied load for a given scheme, the ratio $|\sigma_\omega|/|\sigma_{bend}|$ at the governing cross-sectional point can be evaluated for the other three schemes without repeating the finite-element or shell verification, using the critical bimoment already tabulated in Table 3. Table 7 reports this generalisation for Section H at $L$ = 400 cm.

The reference case illustrated (Scheme A) is therefore, for Section H, the least severe of the four schemes in this respect, not the most severe: neglecting the bimoment for the fixed-fixed scheme (B) at the same span would more than double the extreme-fibre stress relative to bending alone. This generalisation reinforces, rather than qualifies, the practical consequence of omitting the bimoment check altogether depends strongly on the structural scheme, and the 24.2% figure should be read as a representative, not a bounding, estimate of that consequence.

## DISCUSSION

### Synthesis

The results of the case study, the parametric applicability study, and the strength-interaction check, taken together, confirm and extend the four contributions set out in the Introduction. The independently verified toolchain built from the closed-form solutions and finite element formulation developed above closed-form solutions cross-checked symbolically and against a purpose-built finite element formulation in the tradition of [6], converging to 0.005% at 64 elements (Table 1) and validated independently across all four schemes to within 0.2% (Table 2) provides a basis for the numerical results that does not rely on either commercial software or on transcription from a single published source. Building on this toolchain, the parametric applicability study shows that the relative error of the bending–bimoment analogy approximation is, to within numerical round-off, a function of the single dimensionless group $k{\cdot}L$ alone (Table 4), and uses this property to construct a

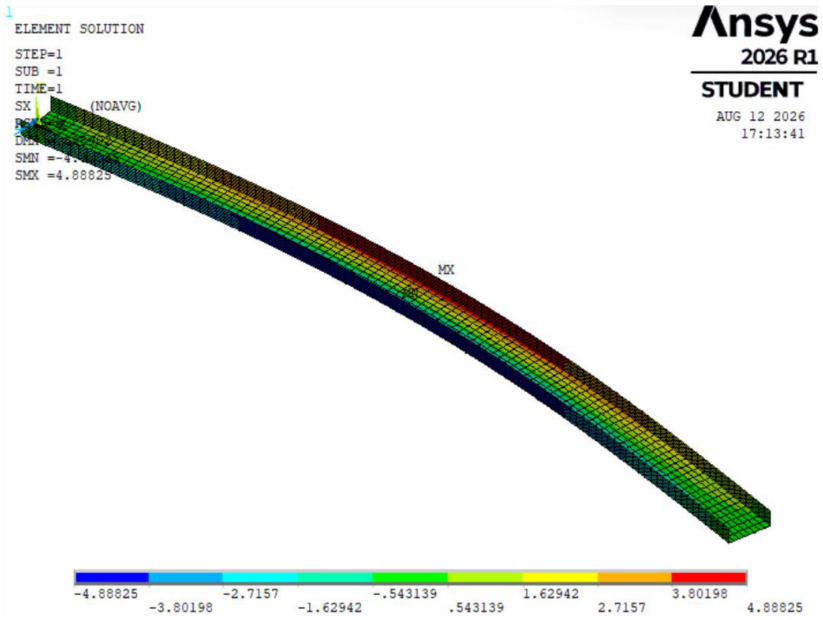



**Figure 8.** Independent ANSYS SHELL181 model: deformed shape and axial stress contour (element solution, unaveraged) for the reference case (Section H, Scheme A, $L$ = 400 cm) under the applied UDL and torque, showing the shell mesh used for verification

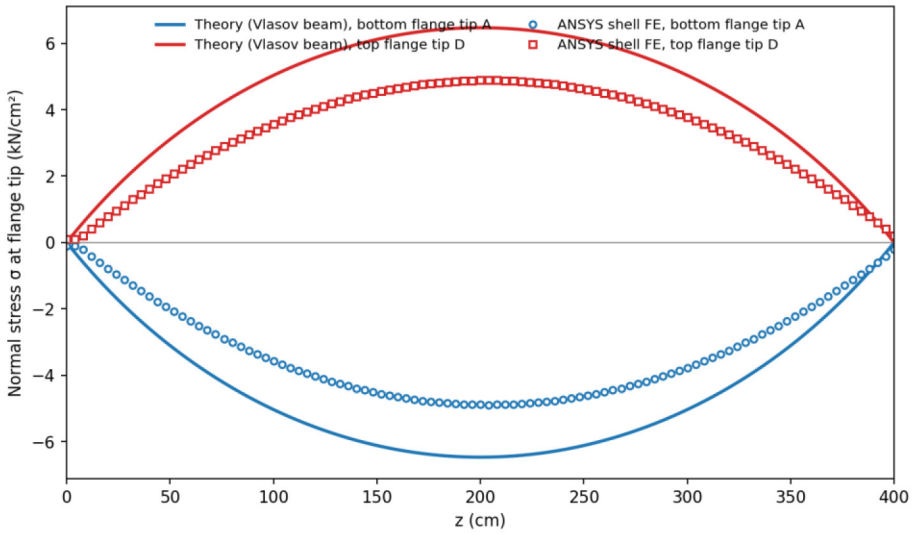



**Figure 9.** Independent ANSYS SHELL181 verification: flange-tip normal stress along the span (Section H, Scheme A, $L$ = 400 cm), shell finite-element results vs. closed-form Vlasov-theory prediction

scheme-resolved applicability chart (Figure 6, Table 5) rather than relying on discrete tabulated cases. Applying that chart to the current tabulated formulation of [13] shows that its reported accuracy (maximum 4.6% over nine schemes) holds specifically because its validation cases lie at $k{\cdot}L$ below roughly 1.6, comfortably inside the limits of Table 5 for three of the four schemes considered here, but already outside the limit for the cantilever case. This is, in effect, a modern re-confirmation, for the current formulation and with independently verified tools, of the degradation Boothby identified in a different tabulated form in 1984 [9]. Finally, the case study and the strength-interaction check show that the practical consequence of the underlying physical effect as distinct from the accuracy of any particular approximation for it is not negligible: a combined stress check that omits the bimoment term altogether overestimates member capacity by 24.2% at the governing cross-sectional point for the reference case considered.

**Table 7.** Overestimate of extreme fibre stress from neglecting the bimoment, all four schemes (Section H, $L$ = 400 cm)

| Scheme | $M_{cr}$ (kN·cm) | $B_{cr}$ (kN·cm²) | Overestimate if B neglected |
|---|---|---|---|
| A – simply supported | 1000.0 | 317.7 | 24.2% |
| B – fixed-fixed | -666.7 | -996.1 | 114% |
| C – cantilever | 4000.0 | -2320.3 | 44% |
| D – point load, mid-span | 2000.0 | 1324.0 | 50% |

## Comparison with prior formulations

Boothby [9] worked with nine tabulated correction curves (stiffness, carry-over and fixed-end-bimoment factors) spanning $L/a$ = 0.5–20, explicitly built to extend the direct analogy into the regime where it degrades, a set of curves subsequently carried into the AISC design guide of Seaburg and Carter [10] and, through it, into decades of routine American design practice and the "bimoment distribution" method built on these curves is, in principle, applicable across the full range covered by Section H in the present study ($k{\cdot}L$ up to 8). Rybakov's formulation [13], by contrast, is a single closed-form correction, Equation 9–10, calibrated implicitly by matching at the critical section rather than by a tabulated distribution procedure, and its published validation is confined to the cold-formed, low $k{\cdot}L$ regime. The present results indicate that Rybakov's formula, applied outside that regime for instance to the hot-rolled Section H would need to be supplemented by a Boothby-type correction [9,10], or replaced by a direct solution of Equation 1, rather than applied directly; the finite element formulation developed earlier offers a lightweight route to such a direct solution that requires neither the tabulated distribution factors of [9,10] nor commercial finite element software, and is considerably simpler than the more general warping-torsion elements now available in the literature [6,7].

## Practical implications

The scheme-dependence identified in the parametric applicability study has a direct bearing on current design practice, and in particular on cold-formed (light-gauge steel framing) construction, the context of the direct strength design philosophy reviewed by Schafer [14] and codified in specifications such as AISI S100 [15] where cantilever purlins and overhangs are common. The applicability limit for the cantilever scheme, $k{\cdot}L \approx 0.74$, is markedly lower than for the other three schemes ($k{\cdot}L \approx 1.8$–$3.2$), so that a blanket statement "the direct bending–bimoment analogy approximation is accurate for cold-formed sections" cannot be relied upon without checking the governing scheme specifically. A designer using Equation 9 for a cold-formed cantilever purlin at a span and section stiffness that would be entirely safe for a simply supported or fixed-fixed member of the same $k{\cdot}L$ may already be outside the 5% tolerance. More generally, the combined strength check shows that the sign of the warping stress relative to the bending stress is not uniform across the cross-section: at the flange-web junctions it is favourable (conservative to neglect), while at the flange tips, which, for an open channel, are also frequently the points of maximum bending stress, it is unfavourable. This combination is what makes neglecting the bimoment altogether, rather than merely approximating it inaccurately, the more consequential practical risk identified in this study.

## Limitations

Several limitations of the present study should be noted. First, the geometric properties of both case-study sections are computed from an idealised uniform-thickness thin-wall centreline model; the comparison against manufacturer catalogue values presented earlier shows this idealisation differs by 7–16% for the torsion-related properties of a hot-rolled channel, a level of deviation that is inherent to classical thin-walled bar theory itself [3,5] and not specific to the bending–bimoment analogy approximation, but that should be kept in mind when the results here are compared against catalogue-based design values.

Second, the cold-formed section considered (Section C) is a plain, unlipped channel of the same overall size as, but not identical to, the lipped profile used in [13]; edge lips increase both $I_d$ and $I_\omega$ and would shift the corresponding $k{\cdot}L$ values, so the

specific numerical results for Section C should not be read as a reproduction of the results in [13], only as an independently computed case at comparable overall proportions. Third, the analysis throughout is linear-elastic, small-deformation, and confined to the four isolated single-span schemes considered; continuous multi-span members, frame action, and the interaction between bimoment-induced stresses and lateral-torsional buckling are outside its scope. Fourth, only channel-type open sections are examined numerically, although the theoretical framework developed above applies to any open thin-walled cross-section for which the sectorial coordinate ω can be computed.

Fifth, a supplementary check of the reference case (Section H, Scheme A, $L$ = 400 cm) against an independent three-dimensional shell finite element model (ANSYS, SHELL181, no warping theory assumed a priori) shows close agreement at the flange-web junctions (points B, C of Table 6: within 2–9% of the beam-theory prediction) but a mesh-independent, systematic reduction of about 24–25% at the free flange tips (points A, D), where the shell model returns roughly ±4.89 kN/cm² against the theoretical ±6.47 kN/cm². Figure 9 shows this reduction scales the entire $\sigma(z)$ curve proportionally along the span rather than being localised. The most plausible explanation is a shear-lag-type effect: a real flange is a flexible plate cantilevering from the web and requires a finite in-plane shear transfer to develop the full theoretical stress out to its free edge, an effect the rigid-cross-section assumption of thin-walled beam theory does not capture. This does not affect the paper's central comparison, computed consistently within the beam-theoretic framework throughout (bending–bimoment analogy formulation and parametric applicability study), but is noted here as a preliminary, single-case observation warranting further investigation.

As a further, independent check of the shell-model finding above, the same reference case (Section H, Scheme A, $L$ = 400 cm) was additionally modelled with CalculiX, an independently developed, open-source finite element code unrelated to the ANSYS model used above, using S4 shell elements over the same idealised centreline geometry. The CalculiX model reproduces the beam-theory bending and warping stress components separately to within 1% at all four cross-sectional points of Table 6 (the bending component differing only through the expected centreline-versus-outer-fibre offset, providing an independent, code-agnostic confirmation that the individual bending and warping stress magnitudes computed from beam theory are correct. A full independent reconstruction of the combined (flange-tip) shell result at additional $k{\cdot}L$ values and schemes beyond this single reference case is left for future work, since it requires careful control of the local, load-line-associated plate bending inherent to a shell idealisation of the applied line load, which is outside the scope of the present verification.

Sixth, the applicability classification of Table 5 depends on $k{\cdot}L$, and k is computed from $I_d$ and Iω, both of which as shown by the 7–16% deviation from catalogue values already discussed for Section H carry a modelling uncertainty inherent to the idealised thin-wall representation of a real rolled or formed section. Because $k = \sqrt{(GI_d/EI_\omega)}$ (Equation 3), a fractional error in each of $I_d$ and $I_\omega$ propagates into $k$ as approximately half their combined relative error; for the 7–16% deviations, this corresponds to a plausible uncertainty in $k$, and hence in $k{\cdot}L$, of order 5–8%. This is inconsequential for members whose $k{\cdot}L$ lies well inside or well outside the limits of Table 5 (e.g. Section H at $k{\cdot}L$ = 8.04, or Section C's Schemes A, B and D at $k{\cdot}L$ = 1.1–1.6), but it is material for a member whose $k{\cdot}L$ falls close to a scheme's applicability limit: Section C's cantilever scheme, at $k{\cdot}L$ = 1.09–1.63, already exceeds its 0.74 limit by a comfortable margin, but a member closer to a boundary value would need its $k{\cdot}L$ verified against catalogue, rather than idealised, section properties before either accepting or rejecting the direct bending–bimoment analogy approximation on the basis of Table 5 alone.

## Future work

The applicability chart developed above could be extended to Boothby's original nine-scheme set [9] and to continuous (multi-span) members, for which the interaction between adjacent spans is expected to modify the effective boundary condition at internal supports and hence the applicable $k{\cdot}L$ range. The finite element formulation developed earlier, being independent of both the closed-form solutions used for verification here and of commercial software, provides a natural basis for such an extension, as well as for future work coupling the present linear warping-torsion formulation with lateral-torsional buckling and with material and geometric nonlinearity, along the lines of the more general secondary-torsion

and boundary-element formulations reviewed in [7] or the generalised beam theory (GBT) framework surveyed in [8], which would additionally allow local and distortional cross-section deformation modes to be captured within the same applicability-chart approach.

Regarding the continuous multi-span extension proposed above, the boundary-condition interpretation suggests a qualitative answer to how the applicability limits of Table 5 would shift: an interior support of a continuous member typically provides only partial warping restraint, intermediate between the fork and fixed idealisations used here, while continuity couples the twist and its derivative across the support in a way that is structurally closer to the two-boundary-layer behaviour of Schemes A and B than to the single-boundary-layer behaviour of the cantilever (Scheme C). On this basis, continuity and partial warping restraint at internal supports would be expected to raise, rather than lower, the applicability limits established here, bringing continuous-span members closer to the more favourable A/B-type limits ($k{\cdot}L \approx 1.8$–$3.2$) than to the more restrictive cantilever limit ($k{\cdot}L \approx 0.74$), but this expectation is qualitative only and would need to be confirmed by the finite element formulation, extended to an assembled multi-span model with the appropriate continuity conditions at interior supports.

## CONCLUSIONS

This study has re-examined the applicability of the direct bending–bimoment analogy for restrained torsion of open thin-walled steel members, using an independently verified toolchain and four representative structural schemes. The main conclusions are:

1. An independent verification toolchain was assembled without recourse to commercial finite element software: closed-form solutions for four classical schemes were re-derived symbolically and confirmed to agree exactly with the corresponding published results, and a purpose-built two-node, cubic-Hermite finite element for the governing fourth-order equation was shown to converge monotonically to the exact solution, reaching 0.005% error at 64 elements.
2. The relative error of the direct bending–bimoment analogy approximation, $\varepsilon(x)$, was shown by direct numerical demonstration to be a function of the single dimensionless group $k{\cdot}L$ alone, independent of section geometry, material properties, and load magnitude, a conclusion verified numerically by confirming agreement between two unrelated sections at matched $k{\cdot}L$ to within $2 \times 10^{-4}$ percentage points.
3. This universal relationship was used to construct a scheme-resolved applicability chart. The approximation exceeds a 5% tolerance beyond $k{\cdot}L \approx 0.74$ for cantilever members, and beyond $k{\cdot}L \approx 1.8$–$3.2$ for simply supported and fixed-fixed members under distributed or mid-span point loading. Applied to the current tabulated formulation of the method, this confirms for that formulation specifically, and with independently verified tools, the same degradation with increasing $k{\cdot}L$.
4. Evaluating the four schemes on both a hot-rolled channel ($k{\cdot}L \approx 8$) and a cold-formed channel ($k{\cdot}L \approx 1.1$–$1.6$) showed that the applicability boundary is scheme-dependent: three of the four schemes remain within tolerance for the cold-formed section at ordinary purlin spans, but the cantilever scheme does not, even at the shorter span considered. Because cantilever cold-formed members (overhangs, cantilevered purlins) are common in practice, this scheme-dependent sensitivity has direct practical relevance and does not appear to have been highlighted in prior applicability studies of the method.
5. A representative combined strength check showed that the practical consequence of the underlying physical effect exceeds the accuracy question addressed above: omitting the bimoment term from the strength check altogether, a gap left open by codes that require the check without specifying how B is to be obtained overestimates the member's capacity by 24.2% at the governing cross-sectional point (the open flange tip) for the reference case considered, while being conservative at the flange-web junctions.
6. These results indicate that the direct bending–bimoment analogy approximation remains a useful design tool within the scheme-specific $k{\cdot}L$ limits established here, but that its use outside those limits and, more fundamentally, the omission of the bimoment check altogether should be treated as a distinct and, in the case of open-flange-tip stresses, non-conservative source of error in the design of open thin-walled steel members.

## REFERENCES


1. Trahair, N.S.; Bradford, M.A.; Nethercot, D.A.; Gardner, L. The Behaviour and Design of Steel Structures to EC3, 4th ed.; Taylor & Francis: London, UK, 2008. https://doi.org/10.1201/9781315273518
2. Timoshenko, S.P. Theory of bending, torsion and buckling of thin walled members of open cross section. J. Frankl. Inst. 1945, 239(3), 201–219.
3. Vlasov, V.Z. Thin-Walled Elastic Beams, 2nd ed.; Israel Program for Scientific Translations: Jerusalem, Israel, 1961 (translated from the 1959 Russian original).
4. Bychkov, D.V. Structural Mechanics of Thin-Walled Bar Structures; Gosstroyizdat: Moscow, USSR, 1962.
5. Gjelsvik, A. The Theory of Thin Walled Bars; John Wiley & Sons: New York, NY, USA, 1981.
6. Friberg, P.O. Beam element matrices derived from Vlasov's theory of open thin-walled elastic beams. Int. J. Numer. Methods Eng. 1985, 21, 1205–1228.
7. Sapountzakis, E.J. Bars under torsional loading: A generalized beam theory approach. ISRN Civ. Eng. 2013, 2013, 916581.
8. Mittelstedt, C. Generalized beam theory for the analysis of thin-walled structures -a state-of-the-art survey. Thin-Walled Struct. 2024, 200, 111849.
9. Boothby, T.E. Application of flexural methods to torsional analysis of thin-walled open sections. Eng. J. AISC 1984, 21(4), 189–198.
10. Seaburg, P.A.; Carter, C.J. Steel Design Guide 9: Torsional Analysis of Structural Steel Members; American Institute of Steel Construction: Chicago, IL, USA, 1997.
11. Montoya-Vargas, S.; Aristizabal-Ochoa, J.D. Torsion of prismatic I-beams with partially restrained warping at the end supports: Bending analogy method. Eng. Struct. 2019, 180, 621–629. https://doi.org/10.1016/j.engstruct.2018.11.067
12. Aguero, A.; Glauz, R.; Almerich-Chulia, A.; Kolekova, Y.; Martin-Concepcion, P. Resistance of steel sections (Classes 1 to 4) including bimoment effects. Buildings 2025, 15, 3894. https://doi.org/10.3390/buildings15213894
13. Rybakov, V.A. Stress-Strain State and Load-Bearing Capacity of Light Steel Structures under Restrained Torsion. Doctoral Dissertation (Dr. Sc.), Peter the Great St. Petersburg Polytechnic University, St. Petersburg, Russia, 2024.
14. Schafer, B.W. Review: The direct strength method of cold-formed steel member design. J. Constr. Steel Res. 2008, 64, 766–778.
15. AISI S100-16. North American Specification for the Design of Cold-Formed Steel Structural Members; American Iron and Steel Institute: Washington, DC, USA, 2016.
16. Polinkevich, K.Yu. Determination of the Stress-Strain State of Thin-Walled Anisotropic Open-Profile Rods under Torsion. Candidate Dissertation, Saint Petersburg State University of Architecture and Civil Engineering, St. Petersburg, Russia, 2019.
17. TCVN 5575:2024. Steel Structures - Design Standard; Ministry of Construction: Hanoi, Vietnam, 2024.
18. SP 16.13330.2017. Steel Structures (Updated Edition of SNiP II-23-81*); Ministry of Construction, Housing and Utilities of the Russian Federation: Moscow, Russia, 2017.
19. EN 1993-1-1:2005. Eurocode 3: Design of Steel Structures - Part 1-1: General Rules and Rules for Buildings; European Committee for Standardization (CEN): Brussels, Belgium, 2005.
20. Przemieniecki, J.S. Theory of Matrix Structural Analysis; McGraw-Hill: New York, NY, USA, 1968 (reprinted Dover Publications, New York, NY, USA, 1985).
21. Gorynin, A.G.; Gorynin, G.L.; Golushko, S.K. Study of restrained torsion of thin-walled open-section beams using the asymptotic splitting method. J. Appl. Mech. Tech. Phys. 2024, 65(3), 502–518.
22. Kharghani, N.; Mittelstedt, C. Global-local-distortional buckling of shear-deformable composite beams with open cross-sections using a novel GBT-ritz approach. J. Compos. Sci. 2025, 9(11), 608. https://doi.org/10.3390/jcs9110608
23. Hung, I.; Kim, C.; Papangelis, J. Bending, torsion and flexural-torsional buckling of back-to-back cold-formed steel channels. Adv. Struct. Eng. 2025, 28(6), 975–993. https://doi.org/10.1177/13694332241300665
24. Kostopoulos, C.; Marzok, A.; Waisman, H. Topology optimization of beams' cross-sectional properties considering torsional and warping behavior. Struct. Multidiscip. Optim. 2025, 68(2), 28. https://doi.org/10.1007/s00158-024-03952-2
25. Piotrowski, R.; Szychowski, A. The elastic critical moment of lateral torsional buckling of steel beams with spatially elastically restrained at the support Nodes. Materials 2026, 19(1), 120. https://doi.org/10.3390/ma19010120